International Journal of Heat and Fluid Flow 50 (2014) 188–200

Contents lists available at ScienceDirect

International Journal of Heat and Fluid Flow

journal homepage: www.elsevier.com/locate/ijhff

Investigation of the mixing layer of underexpanded supersonic jets by particle image velocimetry

Benoît André [a], Thomas Castelain [a,b,*], Christophe Bailly [a,c]

[a] Ecole Centrale de Lyon, Université de Lyon, Laboratoire de Mécanique des Fluides et d'Acoustique, UMR CNRS 5509, 36, avenue Guy de Collongue, 69134 Ecully Cedex, France
[b] Université Lyon 1, 43 Boulevard du 11 Novembre 1918, 69622 Villeurbanne Cedex, France
[c] Institut Universitaire de France, 103 bd Saint-Michel, 75005 Paris, France

ARTICLE INFO

Article history:
Received 18 November 2013
Received in revised form 19 June 2014
Accepted 6 August 2014
Available online 12 September 2014

Keywords:
Underexpanded supersonic jets
Particle image velocimetry
Turbulence
Broadband shock-associated noise

ABSTRACT

The present experimental study focuses on some properties of the turbulence and the shock-cell structure in underexpanded supersonic jets, which are of practical relevance in air transport. Choked jets at fully expanded Mach numbers $M_j = 1.10$, 1.15, 1.35 and 1.50 are investigated using particle image velocimetry. The strength of the shock-cell structure is studied from mean velocity profiles, both in the jet core and in the mixing layer. The general geometry of the latter and its location relatively to the mean shock-cell structure are established. Furthermore, detailed accounts of mixing layer thickness, turbulence levels, spatial correlations and intrinsic turbulence length scales are given. While the mean velocity variations related to the shock-cell structure extend up to the subsonic part of the studied jets, their mixing layer is found to be mostly located in the subsonic region. Some of the observed turbulence properties, like the mixing layer thickness and turbulence levels, are close to what is found for subsonic jets. The effect of the shock-cell structure on turbulence is however visible for $M_j \geqslant 1.35$. The spatial correlations of turbulence are used to estimate intrinsic turbulence length scales and these are found to be of the order of the shock-cell length. These data are used to make some comments upon the generation mechanism of shock-associated noise, a noise component produced by imperfectly expanded supersonic jets.

1. Introduction

A large part of the current commercial aircraft is powered by a high-bypass-ratio engine, in which a hot primary stream is embedded in a cold secondary (fan) flow. At the typical subsonic cruise conditions, the secondary jet becomes underexpanded, meaning that the pressure in the nozzle exit plane is greater than the ambient pressure. This situation induces a shock-cell structure inside the flow, which brings the jet pressure down to the ambient pressure through a pattern of expansions and compressions. Another particularity of such flows compared to subsonic jets is the emission of a specific noise component called the shock-associated noise. This is made up of a tonal part, also known as screech, and a broadband part.

The shock-cell structure of underexpanded jets was much studied experimentally, especially through extensive static pressure measurements (Norum and Seiner, 1982; Norum and Shearin, 1988), and also by the authors of the present paper (André et al., 2014). However, detailed accounts of the turbulence in such jets are scarce. Seiner and Norum (1980) measured turbulence levels and spectra using a hot film probe. Panda and Seasholtz (1999) obtained the coherent part of the density fluctuations in choked jets using the Rayleigh scattering technique and related this to the screeching process. Several studies applied particle image velocimetry (PIV) to these flows. Jerónimo et al. (2002) investigated the first shock cell of an overexpanded jet showing a Mach disc. Alkislar et al. (2003) separated the random from the coherent turbulent motion in the mixing layer of a screeching rectangular jet using stereoscopic PIV, and pinpointed the relation between coherent vortices and screech generation. Bridges and Wernet (2008) applied high-speed PIV to screeching and non-screeching supersonic jets, mainly focusing on turbulence spectra.

The objective of the present experimental study is to focus on some properties of the turbulence and the shock-cell structure in the mixing layer of underexpanded supersonic jets using particle image velocimetry. To begin with, the strength of the shock-cell structure in the mixing layer is estimated. Then, a study of the turbulence of these jets is reported. It addresses the overall structure of the mixing layer, its thickness, turbulence levels, spatial correlations and turbulence length scales in the convected frame. In the

* Corresponding author. Address: Centre Acoustique, Ecole Centrale de Lyon, 36, avenue Guy de Collongue, 69134 Ecully Cedex, France. Tel.: +33 4 72 18 60 15.
E-mail address: thomas.castelain@ec-lyon.fr (T. Castelain).

http://dx.doi.org/10.1016/j.ijheatfluidflow.2014.08.004
0142-727X/

concluding remarks, some comments upon the generation mechanism of shock-associated noise are made in light of the obtained data.

2. Experimental methods

The facility employed in the present work has already been used to study single-stream supersonic jets (André et al., 2014) as well as co-axial jets (André et al., 2011). The configuration considered here is the latter one, with the outer stream set at a Mach number of 0.05 to seed the surroundings of the inner, supersonic jet, during the PIV measurements.

The supersonic jet flow originates from a continuously operating compressor mounted upstream of an air drier. It exhausts through a round, contoured and convergent nozzle of diameter $D = 38.7$ mm. Since the underexpanded jets exiting typical turbofan engines of civil aircraft do not seem to emit the tonal component of shock-associated noise (screech noise), and considering that this component has a strong impact on the jet dynamics (André et al., 2012; André et al., 2013), it appears relevant to eliminate it in the small-scale study. For that purpose, a screech-suppressing nozzle is employed, showing shallow notches carved into its lip. As indicated in André et al. (2013), this nozzle non-intrusively suppresses screech. The reservoir temperature T_t is measured upstream of the exit. Here, the jets are unheated and $T_t \approx 30$ °C. The nozzle pressure ratio (NPR), defined as the ratio between jet stagnation pressure and ambient pressure, is set by measuring the wall static pressure fifteen nozzle diameters upstream of the exit. In the following, results for jets of ideally expanded Mach numbers $M_j = 1.10$, 1.15, 1.35 and 1.50 are presented, corresponding to NPR = 2.14, 2.27, 2.97 and 3.67, respectively. The convective Mach numbers M_c of these jets are 0.49, 0.51, 0.59 and 0.63 for increasing M_j.

A conventional Z-type schlieren system is used to visualise the flow. It consists of a light-emitting diode, two 203.2 mm-diameter f/8 parabolic mirrors, a straight knife-edge set perpendicular to the flow direction and a high-speed Phantom V12 CMOS camera.

Particle image velocimetry has also been applied to measure velocity in a plane containing the jet axis and a notch. Illumination is provided by a pulsed double-cavity Nd:YLF Quantronix Darwin Duo laser and the sheet thickness is 1.7 mm (±0.3 mm). The supersonic jet is seeded with olive oil by means of custom-designed Laskin nozzle generators. The mean particle size is known to be around 1 μm. The secondary flow is seeded by smoke. Both seeding devices are mounted far enough upstream of the exit so that the particle concentration in each flow is approximately uniform. Two CMOS cameras of sensor size 1280×800 pixels^2 are set side by side to double axially the field of view available, which covers a length of about two jet diameters. In the radial direction, only one half of the jet is visualised, since the other part can be deduced by axisymmetry. The PIV set-up is mounted on a frame which can be translated in the jet direction; an axial extent of $12D$ is studied here, meaning that the entire field has been acquired in six parts. For each new location of the frame, a calibration of the camera images is performed using a three-dimensional LaVision plate, the jet operating conditions are reset and 2000 image pairs are recorded. The acquisition frequency of the image pairs is 500 Hz and the magnifying factor for each camera is about 0.05 mm.pixel^{-1}. The delay between the images of each pair is set to 3 μs for all jet conditions. Vector field calculation is performed by a multigrid FFT-based technique using the LaVison DaVis 7.2 software. In all but the last iteration of the velocity computation procedure, the calculation is a two-step process; a 25%-overlap of the interrogation windows is set and no window ponderation is used. For the last iteration, three computational steps are set, as well as a 50%-overlap and an isotropic Gaussian window ponderation. The final correlation windows are of size 8×8 pixels^2, leading to a vector density of one every 0.2 mm, or approximately 190 vectors across the supersonic jet diameter.

The behaviour of the seeding particles in imperfectly expanded jets was studied by André et al. (2014) from laser Doppler velocimetry (LDV) data. It was concluded that the particles followed accurately the flow in slightly underexpanded jets and even in the presence of a Mach disc. The mean velocity results obtained by PIV were compared to LDV profiles and a good agreement was found; the latter technique was validated in André et al. (2014). Our results were also found to be in good agreement with RANS simulations performed during a companion study (Henry et al., 2012).

In the following, the origin of the coordinates is taken on the jet axis, in the nozzle exit plane. The variable x will denote the axial direction and y the transverse direction.

3. Results

In order to introduce the shock-cell structure typical of underexpanded supersonic jets, spark schlieren images of two jets at $M_j = 1.10$ and 1.50 are presented in Fig. 1. Owing to the orientation of the knife-edge in the schlieren set-up, axial gradients of density are visualised here. The well-known quasi-periodic shock-cell pattern is visible. The light (dark) regions correspond to expansion (compression) regions, see Panda and Seasholtz (1999) and André et al. (2014) for more details about the mean shock-cell pattern. At $M_j = 1.50$, a small normal shock, called Mach disc, forms in the first shock cell. Turbulent fluctuations are also visible in these pictures. The fact that they even appear in the jet core region is a result of the integration of the density gradients across the entire jet. Other schlieren images of such jets, also with different knife-edge orientations, can be found in Powell (1953), Seiner and Norum (1979) or Panda (1999), among others.

3.1. Shock-cell structure in the mixing layer

Usually, pressure measurements are used for quantifying the strength of the mean flow gradients (Norum and Seiner, 1982; Norum and Shearin, 1988) but they are generally confined to the jet core. We focus here on the mean flow gradients near the mixing layer. To that end, the velocity gradients in the mixing layer are deduced from the mean velocity maps obtained by PIV, and compared to those existing in the jet core. The extreme values of M_j, namely 1.10 and 1.50, are considered.

A map of mean velocity for $M_j = 1.10$ is presented in Fig. 2, along with calculated mean flow streamlines. The mean velocity on these streamlines, which are almost straight at this low underexpansion, is shown in Fig. 3(a), while the computed gradients of the mean velocity along the streamlines are displayed in (b). It is visible that the gradients wear off when moving downstream or toward the mixing layer and that they remain small in the entire flow. It is also worth noting that the gradients are still present in the subsonic region of the jet.

The flow with $M_j = 1.50$ is now studied. The cartography of the mean velocity is displayed in Fig. 4. The streamlines present a curvature, which comes from the lateral expansions and constrictions of the jet plume, induced by the stronger underexpansion. Because of strong gradients both in the axial and radial directions in the Mach disc region, the velocity estimates from the particle image analysis are there only approximate. The velocity on the jet centreline is nonetheless shown in order to compare the estimated strong gradients associated with the Mach disc with those observed elsewhere in the jet. A signature of the Mach disc is the

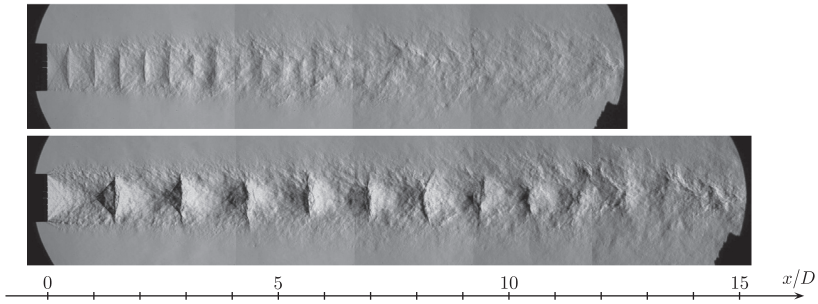

Fig. 1. Schlieren images of two jets at $M_j = 1.10$ (top) and 1.50 (bottom). Each picture is made up of several uncorrelated spark images (exposure time of 4 μs) recorded at different axial locations. The notches cut into the nozzle lip explain the ejections visible at the exit, especially for $M_j = 1.50$.

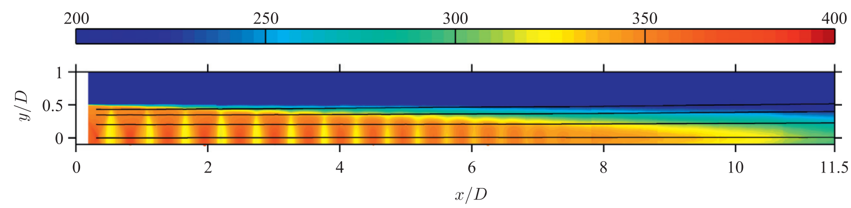

Fig. 2. Cartography of the mean velocity $u = \sqrt{\overline{u_1}^2 + \overline{u_2}^2}$ (m s^{-1}) for $M_j = 1.10$ (u_1 and u_2 are the longitudinal and transverse velocity components, respectively, and the overbar denotes the ensemble averaged value). The horizontal lines represent mean flow streamlines.

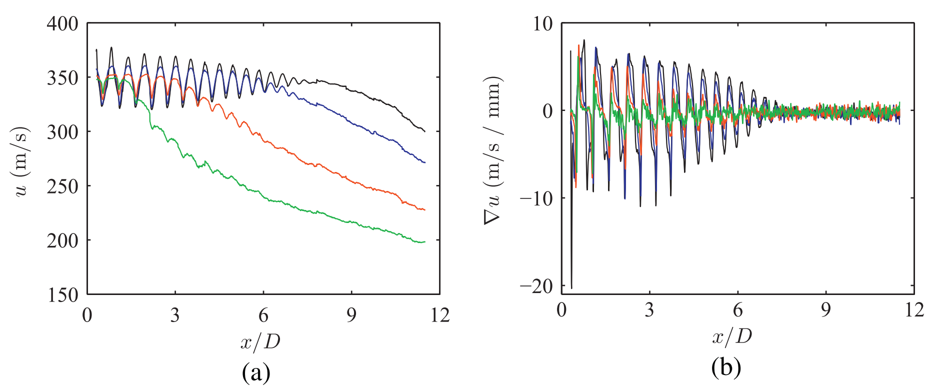

Fig. 3. (a) Mean velocity profiles measured on the mean streamlines depicted in Fig. 2, (b) velocity gradients calculated along the same streamlines; $M_j = 1.10$. The radial stations of the streamlines at their upstream location are $y/D = 0$ (—), 0.2 (—), 0.35 (—), and 0.43 (—).

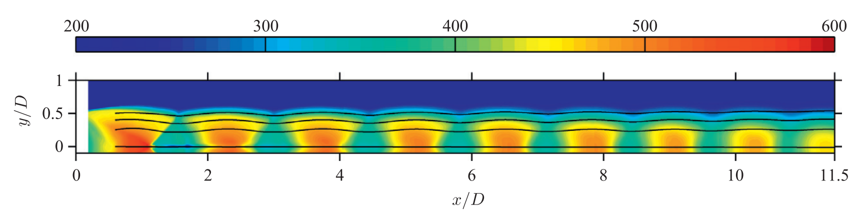

Fig. 4. Cartography of u (m s^{-1}) for $M_j = 1.50$. The horizontal lines represent mean streamlines.

strong negative peaks on the black curve in Fig. 5(b). For the other streamlines, the gradients are also sharp in the first shock cell due to the oblique shock attached to the Mach disc. However, they quickly become weaker downstream. In the second shock cell already, they are larger than, but have the same order of magnitude as, in the case $M_j = 1.10$.

3.2. Turbulence in the mixing layer

The remainder of the paper focuses on the properties of turbulence in the investigated jets. It has to be noted that such small-scale jets naturally sustain a large-scale oscillation due to the screech noise (André et al., 2011) so that it is usually relevant to separate the random fluctuations from the organised, highly energetic, ones (Alkislar et al., 2003). Here, this analysis is not needed since the screech tones, and so the associated oscillations, are suppressed, as was mentioned in Section 2.

3.2.1. General structure of the mixing layer

To begin with, an overview of the structure of the mixing layer is proposed. The mixing layer centre and boundaries are determined and compared to the mean flow pattern.

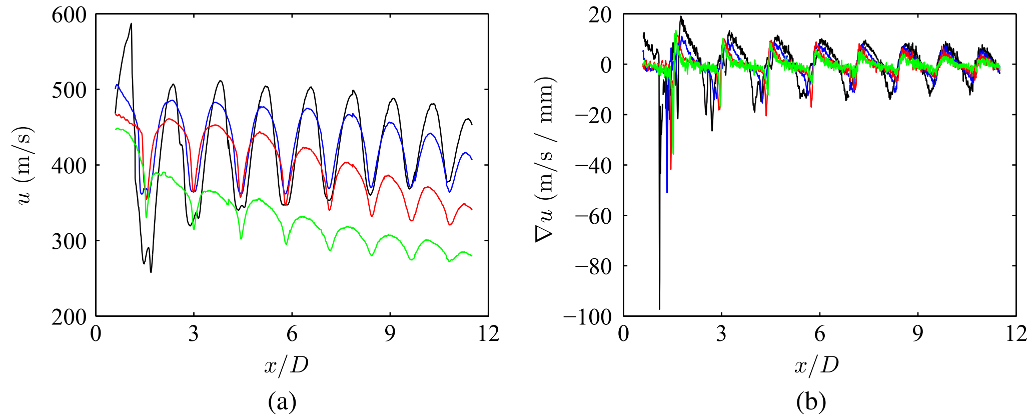

Fig. 5. (a) Mean velocity profiles measured on the mean streamlines depicted in Fig. 4, (b) velocity gradients calculated along the same streamlines; $M_j = 1.50$. The radial stations of the streamlines at their upstream location are $y/D = 0$ (—), 0.25 (—), 0.4 (—), 0.5 (—).

The mixing layer centre is simply determined as the location where the axial velocity fluctuations are the strongest. So as to properly define the mixing layer boundaries, the fluctuation data obtained by the PIV are used. For each axial station, the radial location of the maximum root-mean-square value of the axial velocity fluctuations is determined. In the high- and low-velocity side of the flow, the fluctuation minima are searched. For each side, the mixing layer boundary is defined as the location where the root-mean-square velocity has decreased to 0.1 times the difference between the maximum and the minimum of the fluctuations.

In order to have an idea of the location of the mixing layer relatively to the mean flow, it is of interest of knowing which portion of the mixing layer is supersonic and which is subsonic. Local Mach numbers can be inferred from the PIV data if it is assumed that the total temperature is uniform in the jet and equal to the reservoir temperature, by the formula

$$M = \left\{ \frac{u^2}{\gamma r T_t - u^2(\gamma - 1)/2} \right\}^{1/2} \tag{1}$$

where M is the local Mach number, u the mean velocity, T_t the reservoir temperature, $\gamma = 1.4$ and $r = 287.06\ \mathrm{J\,kg^{-1}\,K^{-1}}$. The sonic line (locus of the unit Mach numbers) is then easily deduced and can be used to separate the supersonic part of the mixing layer from the subsonic part. The total temperature uniformity can be assumed because the jets are unheated, meaning that the total temperature inside the supersonic jet is very close to that of the low-speed coflow. Furthermore, it was checked that a possible change in the total temperature only had a limited effect on the results presented in the following.

A map of the jet plume for the operating condition $M_j = 1.10$, combining local Mach number and root-mean-square axial velocity fields, is presented in Fig. 6. Also included on both cartographies are the locations of the mixing layer boundaries, of the mixing layer centre, and of the sonic line (all the lines are symmetric about the jet axis, and the line of the mixing layer centre has been smoothed for better readability). It can be said from this figure that all lines are almost straight; hence, no influence of the shock-cell structure is visible. Furthermore, the inner boundary of the mixing layer reaches the jet axis around $x/D = 9$, which marks the end of the potential core; downstream of this axial station, the mixing layer has grown across the entire jet. The supersonic core, being the region of supersonic flow, extends of course beyond the potential core, up to 10.5 D. Note also that the outer boundary of the mixing layer reaches the outermost measured location near $x/D = 10$, meaning that past this point, the real outer boundary extends actually still further outward than it is shown here. More importantly, it is obvious from Fig. 6 that most of the mixing layer is at subsonic conditions, and that the supersonic part is very thin. In particular, the mixing layer centre lies well inside the subsonic region of the jet. These observations remain true if the transverse velocity fluctuations are considered instead of the axial ones.

Similar results for $M_j = 1.50$ are proposed in Fig. 7. The lines are only drawn on the relevant half for easier reading. Compared to $M_j = 1.10$, the mixing layer centre and the sonic line are clearly undulating periodically, which is related to the succession of lateral expansions and constrictions induced by the stronger underexpansion at this operating condition. Note also the secondary ejection through a notch, visible near the nozzle exit.

A direct comparison between the two jets is proposed in Fig. 8, where the locations of mixing layer centre and boundaries relatively to the sonic line are shown. The locations of the sonic line and of the centre, inner boundary and outer boundary of the mixing layer are denoted by y_s, y_c, y_i and y_o, respectively. The curves are truncated at $x/D = 8$ for $M_j = 1.10$ since the shock-cell structure ends approximately there. It is clearly illustrated by these plots that the mixing layer centre lies in the subsonic part for both jets and that the mixing layer is mostly subsonic. It seems however

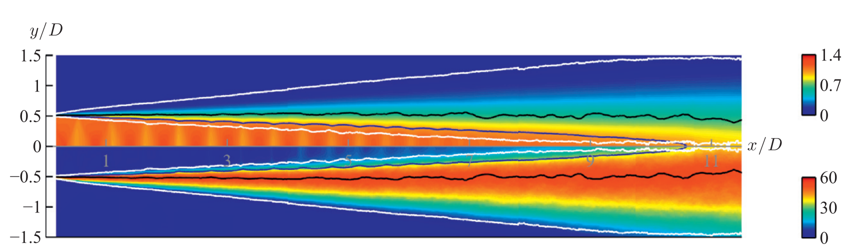

Fig. 6. Combined maps of local Mach number M on the top half and root-mean-square axial velocity fluctuations on the bottom half (in m s^{-1}), $M_j = 1.10$. Superimposed on both maps are: (white lines) mixing layer inner and outer boundaries, (black line) mixing layer center, (blue line) sonic line. For reference, the spatial mean centreline velocity for the supersonic jet is 345 m s^{-1}. (For interpretation of the references to colour in this figure legend, the reader is referred to the web version of this article.)

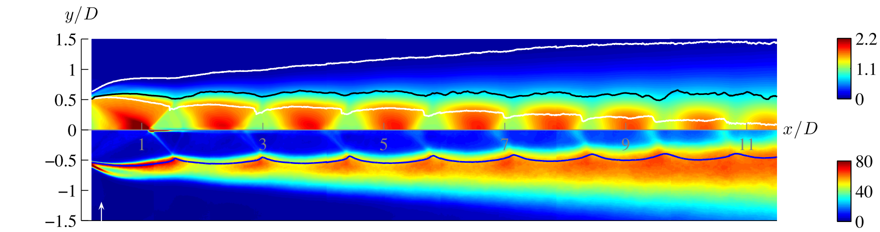

Fig. 7. Same legend as in Fig. 6, but for $M_j = 1.50$. The arrow on the bottom map pinpoints the ejection through the notch contained within the measurement plane. For reference, the spatial mean centreline velocity for the supersonic jet is 423 m s^{-1}.

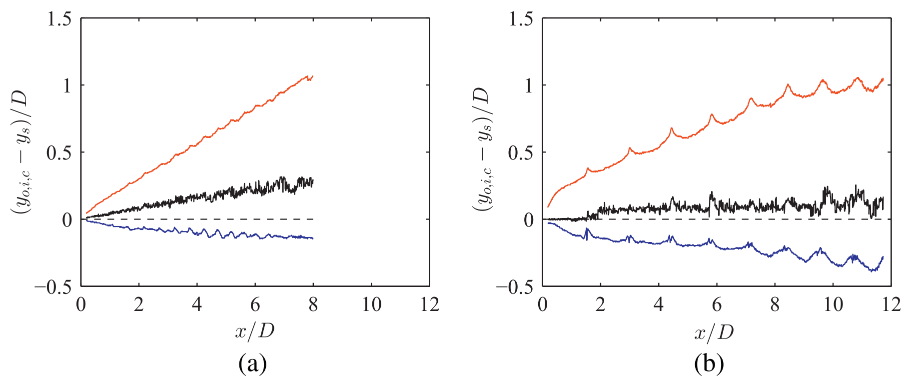

Fig. 8. Location of the mixing layer boundaries and mixing layer centre relatively to the sonic line. (a) $M_j = 1.10$, (b) $M_j = 1.50$. — $(y_c - y_s)/D$, — $(y_i - y_s)/D$, — $(y_o - y_s)/D$. The dashed horizontal line marks the sonic line location ($y = y_s$).

that the three curves tend to move down when M_j is increased, which is confirmed by the results at the intermediate values of M_j (not shown here). This means in particular that the mixing layer centre moves closer to the sonic line for increasing M_j, while the supersonic part of the mixing layer thickens.

An interesting feature of the jet at $M_j = 1.50$ can also be seen in Fig. 7. The axial stations of the turbulence maxima are not perfectly aligned with the end of the mean shock cells. The shift between the upper and lower map of the figure is made clear by the drawing of the sonic line on the lower map: the turbulence maxima are slightly ahead of the mean velocity minima, and even more so when moving downstream. This situation entails deep incursions of pockets of high turbulence intensity inside the supersonic region of the jet. This adds up to the relative closeness of the mixing layer centre to the supersonic region of the jet, as compared to the jet at $M_j = 1.10$, and constitutes a noticeable difference between the jets at $M_j = 1.10$ and $M_j = 1.50$.

3.2.2. Mixing layer thickness

The mixing layer momentum thickness is now assessed, as it is the relevant parameter for studying the stability of shear layers (Michalke, 1965). It will also provide a useful length scale for the following analysis.

Usually, the momentum thickness δ_θ is defined as

$$\delta_\theta = \int_{y_0}^{\infty} \frac{\overline{\rho u_1}}{(\overline{\rho u_1})_0}\left[1 - \frac{\overline{u_1}}{(\overline{u_1})_0}\right] dy \tag{2}$$

for compressible flows (White, 1974). In Eq. (2), ρ and u_1 are the density and the axial component of velocity, y is the radial coordinate and y_0 a reference location. The subscript 0 means that the variables are taken at $y = y_0$ and the overbar denotes the mean value. This definition is used for instance by Ponton and Seiner (1992) and Cheng and Lee (2005) in the case of imperfectly expanded supersonic jets. They define different reference positions y_0 though. Cheng and Lee (2005) perform the integral (2) from the jet axis ($y_0 = 0$). Since the velocity on the axis is not always the maximum velocity of a radial profile owing to the shock-cell structure (typically, near the end of the compression regions), negative contributions will occur in the integral. Therefore, the computed momentum thickness oscillates across the shock cells, and can even take on negative values. In order to avoid this problem, Ponton and Seiner (1992) perform the integration from the radial location of the maximum velocity. However, it happens that the maximum velocity be located well inside the jet, again due to the shock-cell structure (typically, near the end of the expansion regions). In such an event, some integrated components do not belong to the mixing layer and its thickness is overestimated.

The incompressible version of Eq. (2) is employed here, since only the velocity is measured. It reads

$$\delta_\theta = \frac{1}{[\overline{u_1}(y_i) - \overline{u_1}(y_o)]^2} \int_{y_i}^{y_o} [\overline{u_1}(y) - \overline{u_1}(y_o)][\overline{u_1}(y_i) - \overline{u_1}(y)] dy \tag{3}$$

In order to avoid the above-mentioned issues concerning the selected integration limits, they are chosen here as y_i and y_o, the inner and outer mixing layer boundaries defined in Section 3.2.1. In the event that negative contributions to δ_θ would be integrated, which happens when the inner boundary is closer to the jet axis than the velocity maximum in the radial direction, δ_θ is not computed. This explains some blanks in the curves displayed hereafter. In Fig. 9 is shown a comparison between the estimations of δ_θ obtained by the different definitions of the integration limits introduced above. It is clear that integrating over the present boundaries induces a disappearance of the trace of the shock-cell structure altogether and that the evolution of δ_θ becomes linear, for this operating condition.

Another mixing layer thickness can simply be defined as

$$\delta = y_o - y_i$$

It has been found that it closely corresponds to 7.5 times δ_θ for all values of M_j investigated. This relation is exemplified in the case $M_j = 1.10$ in Fig. 10.

The evolution of δ_θ until the end of the potential core of each jet is shown in Fig. 11 for all values of M_j. The extent of the potential core is determined from the centreline mean velocity profiles. Only

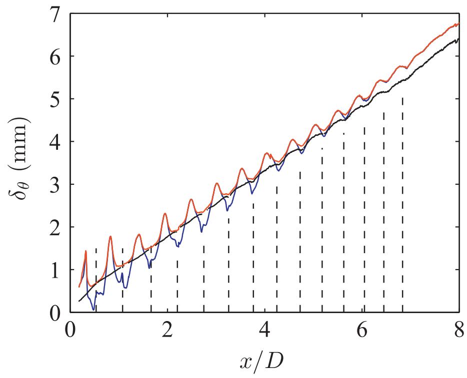

Fig. 9. Comparison of different calculation techniques for δ_θ (M_j = 1.10). For each curve, Eq. (3) is used, with — y_i = 0 and y_o the furthest location acquired, — y_i the location of maximum velocity and y_o the furthest location acquired, — y_i and y_o defined by the method proposed here. The dashed lines mark the end of the shock cells (end of the compression regions).

in the case of M_j = 1.50 does it extend beyond the measured field of view.

Firstly, it has to be noted that in the case of M_j = 1.35 and 1.50, the computation of the outer mixing layer boundary suffers from the limited radial extent of the field of view, as can be seen in Fig. 7: sufficiently far downstream, it is constrained to remain in the measured domain, while it should exit it. This situation should have a limited effect on δ_θ though, for the integrand in Eq. (3) is small near the mixing layer boundaries. The deviation from linearity observed on δ_θ for M_j = 1.35 and 1.50 far enough downstream can probably be explained by this effect. Secondly, it is visible that the very beginning of the mixing layer is thickening at a faster rate than further downstream, and even more so when M_j increases. This is due to the presence of a notch in the measurement plane, which entails a secondary ejection through it and thus a thicker mixing layer (indeed, measurements with a plain nozzle do not show this feature). When M_j is increased, the NPR also becomes larger and the secondary ejection is more pronounced, which explains the larger effect observed at high M_j. Thirdly, the mixing layer growth is linear beyond the first diameter for all conditions, which is characteristic of fully turbulent mixing layers (Troutt and McLaughlin, 1982). The slope of this linear growth decreases when M_j increases. This can be mostly explained by the reduced mixing efficiency induced by increased compressibility (Papamoschou and Roshko, 1988) (compressibility effects are often parametrised by convective Mach numbers, whose values have been indicated for the studied jets in Section 2.). The decrease in mixing layer growth rate entails the well-known potential core lengthening when M_j increases (Lau, 1981). The numerical values of the slopes are gathered in Table 1. As a comparison, the growth rates measured by Fleury et al. (2008) in subsonic jets at Mach numbers of 0.6 and 0.9 are 0.0289 and 0.0265, respectively. The present results are thus consistent with subsonic values. Finally, an effect of the shock-cell structure on the mixing layer thickness can only be identified at the highest underexpansions (M_j = 1.35 and 1.50) in the form of an increase of δ and δ_θ at the end of the shock cells. This cannot be seen on Fig. 11 due to the blanks explained earlier but it is readily visible in Fig. 7.

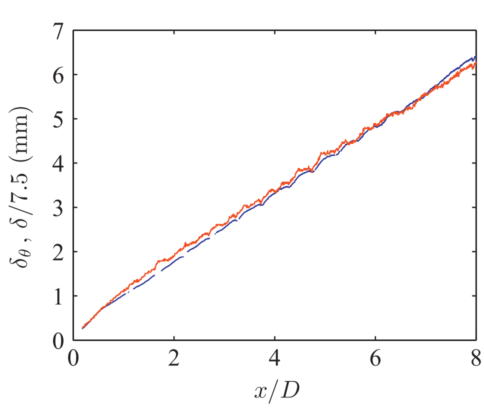

Fig. 10. Relationship between δ_θ and δ, M_j = 1.10. — δ_θ, — $\delta/7.5$.

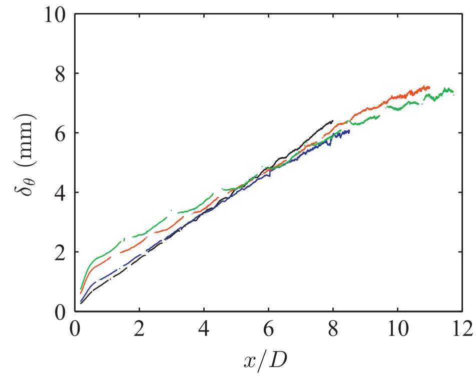

Fig. 11. Evolution of δ_θ with axial distance. — M_j = 1.10, — M_j = 1.15, — M_j = 1.35, — M_j = 1.50.

3.2.3. Turbulence levels

The turbulence levels measured in the mixing layer of the four jets studied are now analysed. Turbulence being mainly produced by velocity gradients, the ratios of the root-mean-square velocity fluctuations (written σ_1 and σ_2 for u_1 and u_2, the velocity components in the longitudinal and transverse direction) over the velocity difference ΔU between the supersonic jet and the low-speed co-flow are formed to provide indicators of turbulence levels. Since underexpanded supersonic jets are not uniform, it is not obvious which velocity is to be considered to compute ΔU. A spatial mean velocity is chosen here, about which the axial velocity oscillates in the shock-cell structure.

Turbulence levels are plotted in the following on the lines of peak fluctuations for u_1. The results for M_j = 1.10 and 1.15 are shown in Fig. 12. The turbulence intensities are seen to be quite flat; the higher values near the nozzle exit are an effect of the notch located in the plane of visualization. They reach 16% for the longitudinal velocity for both conditions, while the levels associated with the transverse component are between 10% and 11%. These values are in good agreement with what is observed in subsonic jets. Davies et al. (1963) measured with a hot wire probe peak turbulence levels of 16% in the mixing layer of round jets of Mach numbers lower than 0.6. Fleury (2006) obtained longitudinal profiles of turbulence intensity which are also flat and show about the same values as the present ones, for jet Mach numbers of 0.6 and 0.9. The results of Jordan et al. (2002) and Kerhervé et al. (2004), obtained by laser Doppler velocimetry for a jet Mach number of 0.9 and in a perfectly expanded jet at M_j = 1.2, respectively, also suggest the same behaviour for the axial evolution of the velocity fluctuations. It seems therefore that the shock-cell

Table 1
Growth rate of δ_θ as a function of M_j.

M_j	1.10	1.15	1.35	1.50
$d\delta_\theta/dx$	0.0199	0.0175	0.0158	0.0141

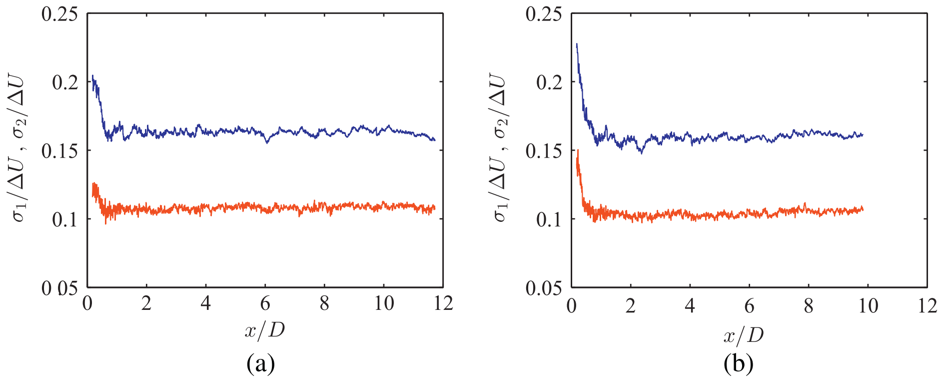

Fig. 12. Longitudinal and transverse turbulence levels in the mixing layer. (a) $M_j = 1.10$, (b) $M_j = 1.15$. — $\sigma_1/\Delta U$, — $\sigma_2/\Delta U$.

structure has little influence on the turbulence levels at these small degrees of underexpansion. This conclusion has already been reached by Seiner and Norum (1980) from the comparison of fluctuation spectra between one underexpanded jet and a fully expanded jet of same M_j.

At $M_j = 1.35$, and even more at $M_j = 1.50$, the line of the maxima of fluctuation in the mixing layer undulates slightly, as it is visible in Fig. 7. The turbulence intensities on the lines of peak values for σ_1 are shown in Fig. 13. In the first shock cell, the fluctuation levels remain approximately constant, before dropping sharply at the beginning of the second shock cell. Still further, the transverse turbulence intensities lie close to 10%, as for the slightly underexpanded jets, but start from a slightly lower value and tend to increase in the downstream direction. As for σ_1, an obvious oscillation of the levels can be observed, where the maxima are reached near the end of the compression regions (but slightly upstream of the shock-cell ends, as pinpointed in the comments of Fig. 7) and the minima occur near the end of the expansion regions (middle of the shock cells). This undulating behaviour is in agreement with the hot film measurements performed by Seiner and Norum (1980), Seiner and Yu (1984) and Seiner et al. (1985) in underexpanded jets, as well as with the numerical simulations included in this latter reference. Bridges and Wernet (2008) found the same evolutions by PIV for the fluctuations of the axial component of velocity. Interestingly, the *maxima* of the axial velocity fluctuations are near 16% for both jets, as is emphasized in Fig. 13 by the horizontal dashed lines. Recalling that it was the levels measured for $M_j = 1.10$ and 1.15, it seems that the shock-cell structure has a role of suppressor of turbulent fluctuations at higher underexpansion. When this structure weakens downstream, the minima of fluctuations accordingly rise while the maxima remain around 16%.

It is interesting to note that Panda and Seasholtz (1999) measure oscillations in the fluctuations of density showing *minima* near the end of the shock cells. Upon examining the profiles of σ_2, a very slight oscillation of these fluctuations appears, but it is opposite to those of σ_1. They would therefore match the modulations of the density fluctuations.

If the oscillation of the turbulence levels related to the shock-cell structure is omitted, their general evolution is quite flat for all values of M_j considered here. Some of the studies quoted earlier confirm this property, but others show a large increase of the fluctuations with downstream distance (Seiner and Norum, 1980; Panda and Seasholtz, 1999; Bridges and Wernet, 2008). This tendency comes from vanishing fluctuation levels near the nozzle exit, which can probably be explained by considering that the turbulence levels are measured on a straight line in these references. For example, the lipline ($y/D = 0.5$), chosen by Seiner and Norum (1980) and, with some modification, by Bridges and Wernet (2008), quickly moves out of the mixing layer for highly underexpanded jets because of the initial lateral expansion of the flow, while it is reached again by the mixing layer further downstream. The same remark holds for the measurements by Panda and Seasholtz (1999), performed on the line $y/D = 0.63$. Furthermore, it is possible that the presence of screech tones in some of these works induces an increase of the fluctuations in the downstream direction.

3.2.4. Spatial correlations

Spatial correlations are computed from the instantaneous velocity fields in order to obtain information on the size, shape and orientation of the turbulent structures in the mixing layer. The coefficient of space–time correlation is written

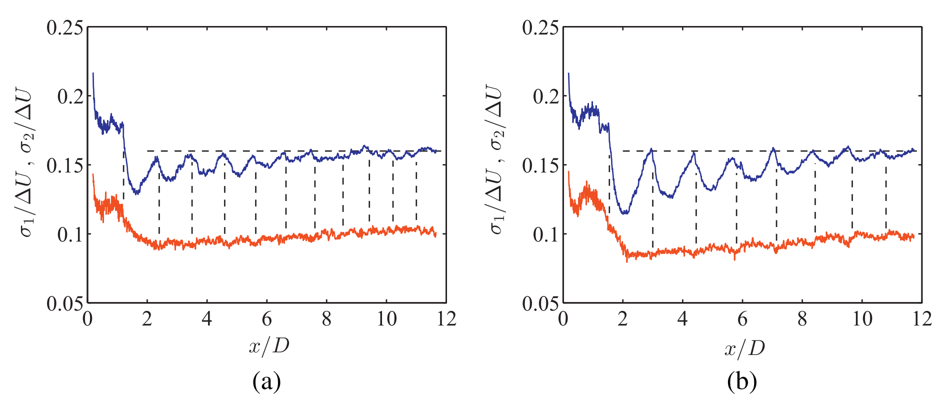

Fig. 13. Longitudinal and transverse turbulence levels in the mixing layer. (a) $M_j = 1.35$, (b) $M_j = 1.50$. — $\sigma_1/\Delta U$, — $\sigma_2/\Delta U$. The vertical lines mark the end of the shock cells; the horizontal lines denote 16%, which is the approximate value of $\sigma_1/\Delta U$ at $M_j = 1.10$ and 1.15.

$$R_{ij}(\boldsymbol{x},\xi,\tau)=\frac{\overline{u'_i(\boldsymbol{x},t)u'_j(\boldsymbol{x}+\xi,t+\tau)}}{\sigma_i(\boldsymbol{x})\,\sigma_j(\boldsymbol{x}+\xi)} \tag{4}$$

where the indexes i and j represent the velocity component, u'_i denotes the fluctuations of u_i, $\boldsymbol{x}$ is the reference point, ξ is the separation vector and τ is the time delay. Ensemble averages are calculated over the 2000 fields acquired. In the following, only spatial correlations are calculated, so that $\tau = 0$.

Cross-correlations R_{11} and R_{22} have been estimated while moving the reference point on the horizontal line $y/D_j = 0.5$, with D_j the fully expanded jet diameter, slightly larger than D. This is done to account for the expansion of underexpanded jets. It has been checked however that the precise location of the reference points did not have a strong influence on the results. Examples of correlation plots are shown in Fig. 14 for $M_j = 1.15$.

From R_{ii}, $i \in (1,2)$, it is possible to calculate the integral length scale of u'_i in the direction k, $k \in (1,2)$, by

$$L_{ii}^{(k)}(\boldsymbol{x})=\frac{1}{2}\int_{-\infty}^{+\infty}R_{ii}(\boldsymbol{x},\xi_k)\mathrm{d}\xi_k \tag{5}$$

where ξ_k is the separation distance in the direction k. In practice, the integration is performed over a finite interval. Here, it is done down to the correlation contour of level 0.1 to avoid the low correlation domain which can be noisy; in any case, the integration limit has no large influence on the numerical values, and it has to be noted that integral length scales are merely order-of-magnitude estimates. The vertical cut ($\xi_1 = 0$) of the correlation coefficient R_{11} shown in Fig. 14(a), is represented in Fig. 15 and the integration domain is emphasized on that curve. It has been checked that the various integral length scales had converged when using 2000 velocity fields for the estimation.

The various length scales for all values of M_j are shown in Fig. 16. They are seen to grow linearly with the downstream distance, as it is the case for subsonic jets (Laurence, 1956; Davies et al., 1963; Fleury et al., 2008). The estimates of $L_{22}^{(2)}$ are noisier than the other ones and seem to show two different slopes. Some data in the curve of $L_{11}^{(1)}$ are missing because no scale estimate is produced when the curve of the coefficient of correlation, an example of which is shown in Fig. 15, is truncated. This is the case near the edges of the fields of view, and this effect becomes more pronounced as the structures grow. Striking resemblances are visible between the different operating conditions. The agreement between the $L_{11}^{(1,2)}$ curves is remarkable, while the scales $L_{22}^{(1,2)}$ grow more slowly when M_j is increased. Furthermore, a small undulation of $L_{11}^{(2)}$ and $L_{22}^{(1)}$ is visible at $M_j = 1.50$. These curves are reproduced in Fig. 17, along with the position of the end of the shock cells. The oscillations seem thus to originate from the stronger shock-cell pattern.

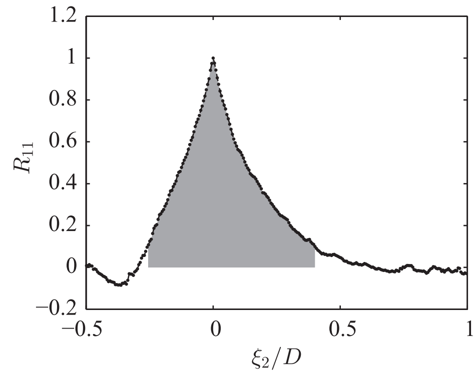

Fig. 15. Transverse profile of the correlation coefficient R_{11} for the case presented in Fig. 14 (a). The shaded area represents the region of integration for determining the integral length scale of turbulence ($L_{11}^{(2)}$ here).

Since the growth of the length scales and the mixing layer thickness is linear, the ratio of the slopes of these quantities is formed. The numerical values are gathered in Table 2 (the scale $L_{22}^{(2)}$ is left out because of the non-uniqueness of the slope). The approximate ratios observed by Fleury et al. (2008) are also recalled. Here as well, $L_{11}^{(1)}/\delta_\theta$ and $L_{11}^{(2)}/\delta_\theta$ are close to 2 and 1, respectively. However, our ratio $L_{22}^{(1)}/\delta_\theta$ is significantly smaller than 1. Furthermore, a noticeable growth of the ratios between $M_j = 1.10$ and 1.50 is identified. This means that the growth rate of the mixing layer thickness decreases quicker with M_j than that of the integral length scales, which is clear when comparing Table 1 and Fig. 16.

The shape of the correlation contours is now examined. The contours shown in Fig. 14 suggest that the turbulent structures have an elliptical shape, which has already been pinpointed by Mahadevan and Loth (1994) or Fleury et al. (2008). In order to quantitatively analyse the contours, ellipses have been fitted to them. The result of this can be viewed in Fig. 14. In the following, only contours of levels 0.3 to 0.8 are considered. Indeed, the contours of lower correlation level are generally more irregular and those of higher correlation are too small for a proper analysis. For each fitted contour, the inclination, the axis sizes and the excentricity of the ellipse have been obtained. The inclination is defined as the angle between the jet axis and the ellipse major axis. Noting a and b the length of the major and minor axes, the ellipse excentricity is

$$e=\frac{\sqrt{a^2-b^2}}{a}$$

e near one means that the ellipse is flat, while $e = 0$ for a circle.

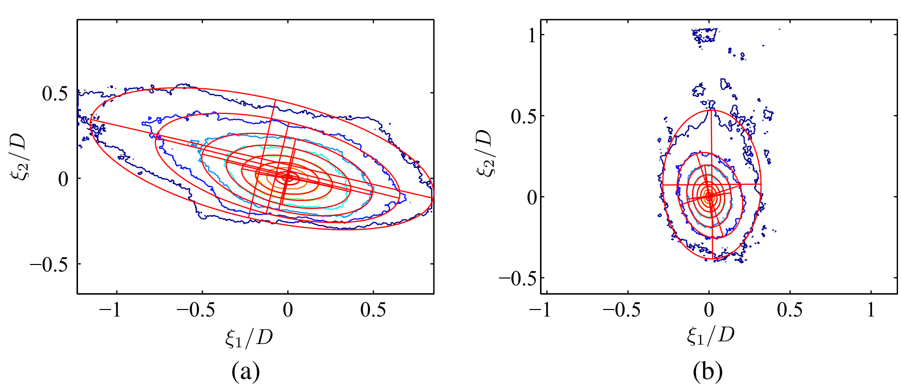

Fig. 14. Correlation contours for $M_j = 1.15$, $y/D_j = 0.5$ and $x/D = 9$. (a) R_{11} ; (b) R_{22}. ξ_i is the separation distance in the direction i. The contours represent the correlation levels 0.1–0.9 in 0.1 step. The elliptical fits, in red, will be used below. (For interpretation of the references to colour in this figure legend, the reader is referred to the web version of this article.)

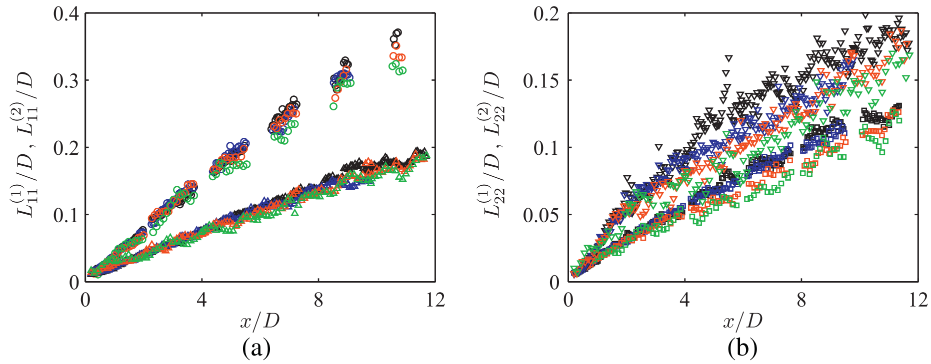

Fig. 16. Integral length scales for all values of M_j, non-dimensioned by the nozzle diameter. (a) $L^{(1)}_{11}$ and $L^{(2)}_{11}$, (b) $L^{(1)}_{22}$ and $L^{(2)}_{22}$. ○ $L^{(1)}_{11}$, △ $L^{(2)}_{11}$, □ $L^{(1)}_{22}$, ▽ $L^{(2)}_{22}$. Black: M_j = 1.10, blue: M_j = 1.15, red: M_j = 1.35, green: M_j = 1.50. (For interpretation of the references to colour in this figure legend, the reader is referred to the web version of this article.)

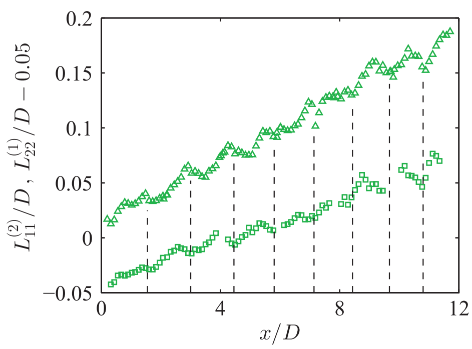

Fig. 17. △ $L^{(2)}_{11}/D$ and □ $L^{(1)}_{22}/D - 0.05$ for M_j = 1.50 (reproduced from Fig. 16). The vertical lines mark the locations of the shock-cell ends.

Table 2
Ratios of the growth rates between the integral length scales and the mixing layer thickness.

	$L^{(1)}_{11}/\delta_\theta$	$L^{(2)}_{11}/\delta_\theta$	$L^{(1)}_{22}/\delta_\theta$
M_j = 1.10	1.76	0.83	0.56
M_j = 1.15	1.95	0.89	0.66
M_j = 1.35	2.06	0.97	0.64
M_j = 1.50	2.15	1.03	0.67
Fleury et al. (2008)	2	1	1

Firstly, the properties of the ellipses as a function of the correlation level are mentioned for M_j = 1.10. The inclination and the minor axis size are shown for R_{11} in Fig. 18. It can be seen that the inclination of the ellipses depends on the correlation level, and decreases (in absolute terms) when the level increases. Mean inclinations span between $-15°$ and $-6.5°$ for the levels 0.3 to 0.8, respectively. The structures are bent toward the high-speed flow, as it has already been noted (Mahadevan and Loth, 1994; Fleury et al., 2008). The minor axis size obviously increases when the correlation level of the contour decreases. When non-dimensioned by the mixing layer momentum thickness, a constant value is found, which is in agreement with the linear growth of the turbulent length scales obtained above. The same features are also true for the major axis (not shown here). The axis lengths deliver another estimation for the size of the turbulent structures. For the contour of level 0.5, the ratios a/δ_θ and b/δ_θ are found to be 3 and 1.4, respectively. Translating this into a fraction of the mixing layer thickness δ ($\delta \approx 7.5\delta_\theta$) leads to ratios of 0.4 and 0.19. Thus, the turbulent structures can be described as *large*, in the acceptance of Papamoschou and Roshko (1988), since their size is of the same order of magnitude as the mixing layer thickness, but they do not extend over its entire width. The excentricity, not shown here, decreases when the correlation level increases, meaning that the contours of higher correlation level are closer to a circle than those of lower level. The excentricity values span from 0.91 to 0.83 for contour levels 0.3 to 0.8.

The results for R_{22} are not shown here for brevity. As compared to the case of R_{11}, the excentricity is smaller and the inclination is close to 90° (see Fig. 14 and Fleury et al., 2008). Also, the axes of the ellipses are smaller, which is in agreement with the relation found between the different integral length scales.

Secondly, the same analysis has been done for the different jets investigated here and some results are compared in Fig. 19. The contour of level 0.5 is chosen. No noticeable difference can be identified between these jets with respect to the excentricity (not shown here) or the *mean* inclination of the ellipses, while a/δ_θ and b/δ_θ tend to decrease when M_j is increased. Here again, the jets of conditions M_j = 1.10 and 1.15 are very similar overall, and no trace of the shock-cell structure can be found in either case. This is not true for M_j = 1.35 and 1.50, where the curves oscillate quasi-periodically. The modulation of the axis lengths reflects that of the integral length scales mentioned above. To understand the oscillation of the inclination, the curve for M_j = 1.50 is plotted in Fig. 20 alongside the inclination of the local mean streamlines going through each point of the y/D_j = 0.5 straight line. The location of the shock-cell ends is also indicated. Both oscillations are in phase with the shock-cell pattern, and we can verify that the inclination of the streamlines goes through 0° at the end of each cell. More importantly, the inclination of the correlation contours relatively to the local streamlines is almost constant. This means that the turbulent structures rotate while being advected by the flow, when the shock-cell pattern is strong enough to induce a notable lateral motion of the mean flow.

3.2.5. Turbulence scales in the convected frame

The intrinsic time scale of turbulence, or time scale in the convected frame of reference, measures the time a structure remains coherent in its motion. It is a very significant piece of information, especially for the broadband component of shock-associated noise (BBSAN). Harper-Bourne and Fisher (1973), who proposed the first model of this noise component, made use of turbulence measurements obtained with the crossed-beam schlieren technique to determine the level of correlation of turbulence from one shock cell to the subsequent ones. They found that the turbulence retained a high level of correlation over several shock cells. They adapted the phased array model developed by Powell (1953) for screech in taking into account this level of correlation between adjacent acoustic sources, supposed to be located at the end of each shock cell. In the end, the sources of BBSAN were thought to partially interfere, which decided the far field directivity. A success of this modelling

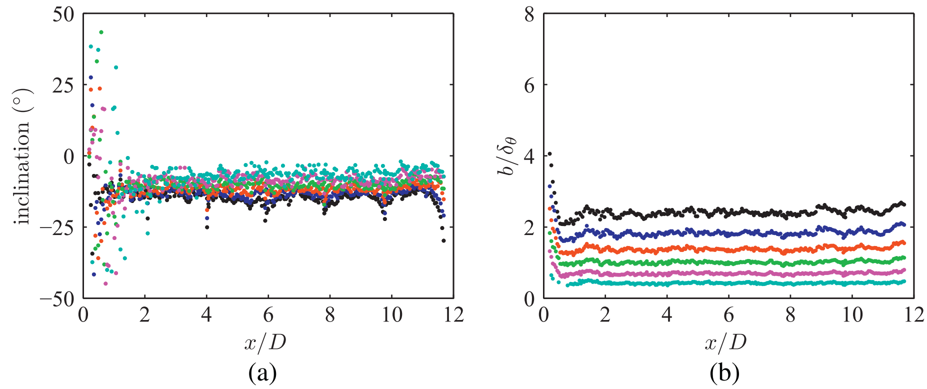

Fig. 18. Evolution of the properties of the ellipses fitted to the correlation contours R_{11} (M_j = 1.10). (a) Inclination, (b) minor axis over δ_θ. Contour levels: ● 0.3, ● 0.4, ● 0.5, ● 0.6, ● 0.7, ● 0.8.

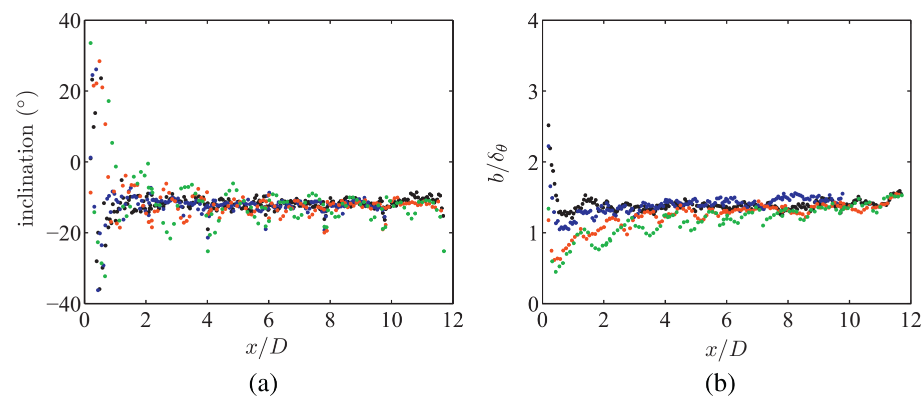

Fig. 19. Properties of the ellipses fitted to the correlation contours R_{11} of level 0.5 for all M_j. (a) Inclination, (b) minor axis over δ_θ. ● M_j = 1.10, ● M_j = 1.15, ● M_j = 1.35, ● M_j = 1.50.

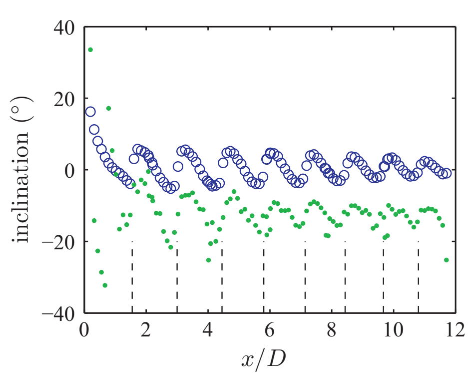

Fig. 20. Evolution of the inclinations of the local mean streamline (○) and of the R_{11}-contour of level 0.5 (●, reproduced from Fig. 19 (a)) along the line y/D_j = 0.5, at M_j = 1.50. The vertical lines mark the end of the shock cells.

is the explanation of the Doppler factor arising in the dependence of the broadband hump peak frequency on the polar angle. Another approach was later proposed by Tam and Tanna (1982) and Tam (1987). It lay on the modelling of turbulence by instability waves, which were supposed to be coherent over many jet diameters. Hence, turbulence coherence over several shock cells is also an important ingredient for this alternative model.

The intrinsic time scale of turbulence has rarely been measured in shock-containing flows, so it is interesting to estimate them and determine the corresponding axial extent of correlation. Such time scales can be defined by

$$T_{cii} = \int_0^{\tau_{0i}} R_{ii}(\boldsymbol{x}, \xi = \boldsymbol{U_c}\tau, \tau)\mathrm{d}\tau \qquad (6)$$

where τ_{0i} is the limit of integration of the coefficient of correlation R_{ii}, $\boldsymbol{U_c}$ is the convection velocity vector, and $i \in (1, 2)$. The acquisition frequency in the present experiment is of course much too low to compute relevant space–time correlation coefficients, so an empirical relation observed for grid turbulence, and checked also by Fleury et al. (2008), has been used. They showed that

$$T_{cii} \approx \frac{L_{ii}^{(1)}}{\sigma_i}$$

for subsonic jets. Both quantities in the right-hand side have been obtained, and owing to the similarities found between the underexpanded jets and subsonic ones, it is believed that such a rule can still be used to estimate the correlation times. The obtained intrinsic time scales T_{c11} are shown in Fig. 21. Lau, 1980, Kerhervé et al. (2004), Panda (2006) and Fleury et al. (2008) measured such a time scale of turbulence in jets and their results are compared here with ours. The values obtained for the supersonic jets are summarised in Table 3. It has to be noted that these jets are *perfectly expanded*. Firstly, the present estimate of T_{c11} decreases with increasing M_j, which is in agreement with the quoted studies. Secondly, our estimates are in very good agreement with the measurements by Lau (1980), but are smaller than those of Kerhervé et al. (2004) and Panda (2006). Anyway, these comparisons prove that the present estimations have the right order of magnitude.

The reader will have noticed that the time scales presented in Fig. 21 and Table 3 are not non-dimensionalised. Such data are sometimes made dimensionless with the nozzle diameter D as

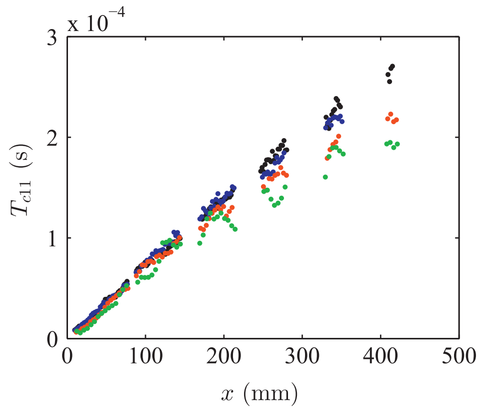

Fig. 21. The time scale in the convected frame T_{c11} against the distance to the nozzle exit for ● M_j = 1.10, ● M_j = 1.15, ● M_j = 1.35 and ● M_j = 1.50.

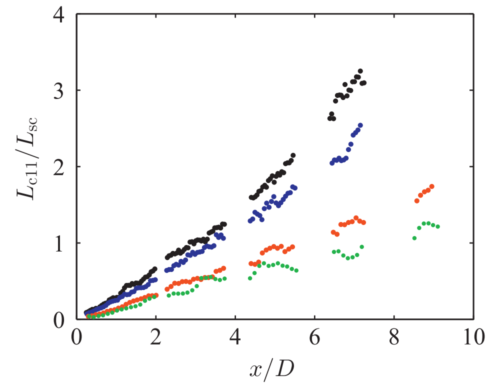

Fig. 22. L_{c11}/L_{sc} against axial location for ● M_j = 1.10, ● M_j = 1.15, ● M_j = 1.35 and ● M_j = 1.50.

Table 3
Values of time scale in the convected frame available in the literature for perfectly expanded supersonic jets. The jets are isothermal for Lau (1980) and unheated for Kerhervé et al. (2004) and Panda (2006). These estimates come from measurements of velocity for Lau (1980) and Kerhervé et al. (2004) and density for Panda (2006).

	M_j	x (mm)	Time scale (μs)
Lau (1980)	1.37	101.6	80
		203.2	120
Kerhervé et al. (2004)	1.2	52	96
		312	299
Panda (2006)	1.4	76.2	75

reference length scale and the ratio D/U_c as reference time scale (Lau, 1980), with U_c being an estimate of the convection velocity of the turbulent structures. However, it is believed that D is not a relevant scale for the early mixing layer. A better one could be the value of δ_θ near the nozzle exit plane, but this value cannot be found in the quoted papers. For further reference, the values of U_c and δ_θ for the present jets are gathered in Table 4. U_c is estimated as $0.7\,U_j$ (Harper-Bourne and Fisher, 1973; Tam and Tanna, 1982), U_j being the perfectly expanded flow velocity; δ_θ is read from Fig. 11 at the middle of the first shock cell, in order to avoid the inaccurate near-nozzle region, which is here also disturbed by the ejections through the notch.

From T_{cii}, a correlation length in the convected frame is estimated by

$$L_{cii} = U_c T_{cii}$$

where U_c is again taken as $0.7\,U_j$. L_{cii} is then non-dimensioned by the local shock-cell length L_{sc}, deduced from the PIV results. Local values of L_{sc} are considered in order to take into account the cell shortening with the axial distance; they are calculated as the mean length of two adjacent cells.

Results for L_{c11}/L_{sc} as a function of the axial location are presented in Fig. 22 for the values of M_j investigated. The curves of L_{c22}/L_{sc} (not presented here) are quite similar, since the ratio L_{c22}/L_{c11} tends to 1/2 a few diameters downstream of the nozzle exit (see also Fleury et al., 2008). The linear increase of $L_{11}^{(1)}$ with

Table 4
Estimates of U_c and measured values of δ_θ around the middle of the first shock cell of each jet, as reference for non-dimensionalising the values of time scale in the convected frame.

M_j	1.10	1.15	1.35	1.50
U_c (m s^{-1})	242	251	284	306
δ_θ (mm)	0.41	0.71	1.51	1.81

x makes L_{c11} rise linearly for all conditions tested, at least initially. For M_j = 1.10 and 1.15, the significant shortening of the shock-cell structure near the end of the pattern is responsible for the steeper rise further downstream. At the higher M_j, the axial extent of measurement did not cover the entire shock-cell structure, which explains the absence of noticeable increase in the slope of L_{c11}/L_{sc}. The important point here is that the rapid increase of L_{sc} with M_j entails a decrease of the ratio L_{c11}/L_{sc}. While it is apparently possible to consider that the turbulent structures remain coherent over several shock cells for low values of M_j, this does not seem to be the case any more for higher Mach numbers, and even less so for values of M_j greater than those investigated in the present experiment. One may argue that the shortening of the shock cells at the very end of the pattern could still allow the turbulent structures to be correlated over several cells, but the shock-cell strength is quite low there and the noise emission should not be as effective. As a consequence, the present results seem to support the suggestion uttered by Pao and Seiner (1983) that the noise mechanism could be different between low and high M_j.

However, since the present estimates merely provide wideband orders of magnitude for the intrinsic time scales of turbulence, it would be of interest to directly measure these time scales in an imperfectly expanded jet in order to refine the results shown here, and gain access to a frequency dependence. Indeed, it is clear from Panda (2006) that in some frequency bands, the lifetime of turbulence can be much larger than the wideband estimate suggests. Therefore, the turbulence may still be coherent over several shock cells at the higher Mach numbers, for a range of frequencies.

4. Concluding remarks

Particle image velocimetry has been applied to four choked jets of fully expanded Mach numbers M_j = 1.10, 1.15, 1.35 and 1.50. The strength of the shock-cell structure has been estimated on mean flow streamlines. It has been found that the velocity gradients inside the jet plume wear off toward the mixing layer and in the downstream direction. In a jet containing a Mach disc, the gradients downstream of the first shock cell have been seen to be of the same order of magnitude as those encountered in slightly underexpanded jets. The velocity gradients have then been found quite moderate everywhere in these flows, and in particular in the region of production of broadband shock-associated noise, which is believed to be approximately located between the third and the eighth shock cell (Seiner and Yu, 1984). Furthermore, velocity gradients typical of the shock-cell structure have still been observed in the subsonic part of the mixing layer.

The main part of this paper focused on the properties of turbulence. Overall, it has been found that slightly underexpanded jets (M_j = 1.10 and 1.15 here) behave very similarly to jets at high subsonic Mach numbers, while the shock-cell structure more noticeably affects jets at higher values of M_j.

The location of the sonic line comparatively to the mixing layer centre and boundaries shows that for all M_j investigated, the layer centre is located in its subsonic part. At low M_j, only a very small portion of the layer is at supersonic condition, while this fraction rises when M_j is increased. Considering that BBSAN comes from the interaction between turbulence and flow gradients, it seems that a non-negligible part of shock-associated noise could be produced in the subsonic region of the mixing layer; for the higher values of M_j, this situation is attenuated by incursions of pockets of turbulence inside the supersonic region of the jet. This belief contrasts with the modellings of the BBSAN mechanism proposed by Harper-Bourne and Fisher (1973), Seiner and Norum (1980) or Seiner and Yu (1984), who explained the shock-associated noise emission by the interaction between oblique shocks and the turbulence in the supersonic part of the mixing layer. Obviously, the above argumentation on the source location of BBSAN is very qualitative. In order to locate the sources of BBSAN more precisely, a volumetric model of the sound sources, like that of Morris and Miller (2010), could be applied after estimation of some of the inputs not provided by our PIV measurements. Other ways of tackling this issue could be by means of acoustic array measurements or correlation between the signal of a probe inside the flow and near field acoustic measurements (Seiner and Yu, 1984).

A simple method, adapted to the particularities of imperfectly expanded supersonic jets, has been presented to compute the mixing layer momentum thickness δ_θ. Its evolution is fairly linear with the downstream distance, like for subsonic jets, and its growth rate decreases with increasing M_j. At the higher values of M_j, the mixing layer has been seen to thicken near the end of each shock cell.

The turbulence levels of slightly underexpanded jets have been found to be approximately constant with downstream distance and very similar to those observed in subsonic jets. For higher M_j values, the first shock cell seems to behave differently, showing higher fluctuation levels. Further downstream, a modulation of the turbulence levels by the shock-cell pattern has been identified, with maxima reached near the cell ends. Comparing these jets to the lower values of M_j, it has been concluded that the cell system acts as a turbulence suppressor.

Spatial correlations of the velocity fluctuations have been computed. A linear growth of the integral length scales has been found. The ratios of the growth rates of these scales to δ_θ take on similar values to those typical of subsonic jets. At high M_j, an undulation of the scales, which is in accordance with the shock-cell structure, has been found. The correlation contours have also been analysed as ellipses. The size of the structures thus defined is of the same order of magnitude as the local mixing layer thickness. At high M_j, a rotation of the turbulent structures in their advection has been observed, which is induced by the shock-cell pattern.

Finally, time scales of turbulence in the convected frame, crucial in connection with the BBSAN generation process, have been indirectly estimated. The corresponding correlation length of the turbulent structures has been found to become increasingly small relatively to the shock-cell length when M_j increases. However, it would be of interest to directly measure these time scales to refine the present conclusion. Especially, a frequency-dependent estimate of the intrinsic length scales of turbulence would be needed to determine if the dependence of L_c/L_{sc} on M_j found from the wideband estimates still holds.

Acknowledgements

The authors wish to thank Airbus Operations SAS (Mauro Porta) and Snecma (Guillaume Bodard) for their joint financial support, as well as Jean-Michel Perrin and Nathalie Grosjean for their help in setting up the experiment and the PIV measurement system.

Appendix A. Supplementary material

Supplementary data associated with this article can be found, in the online version, at http://dx.doi.org/10.1016/j.ijheatfluidflow.2014.08.004.

References

Alkislar, M.B., Krothapalli, A., Lourenco, L.M., 2003. Structure of a screeching rectangular jet: a stereoscopic particle image velocimetry study. J. Fluid Mech. 489, 121–154.
André, B., Castelain, T., Bailly, C., 2011. Experimental study of flight effects on screech in underexpanded jets. Phys. Fluids 23, 1–14.
André, B., Castelain, T., Bailly, C., 2012. Shock oscillations in a supersonic jet exhibiting antisymmetrical screech. AIAA J. 50 (9), 2017–2020.
André, B., Castelain, T., Bailly, C., 2013. Broadband shock-associated noise in screeching and non-screeching underexpanded supersonic jets. AIAA J. 51 (3), 665–673.
André, B., Castelain, T., Bailly, C., 2014. Experimental exploration of underexpanded supersonic jets. Shock Waves 24 (1), 21–32.
Bridges, J.E., Wernet, M.P., 2008. Turbulence associated with Broadband Shock Noise in Hot Jets. NASA Technical Memorandum 215274.
Cheng, T.S., Lee, K.S., 2005. Numerical simulations of underexpanded supersonic jet and free shear layer using WENO schemes. Int. J. Heat Fluid Flow 26 (5), 755–770.
Davies, P.O.A.L., Fisher, M.J., Barratt, M.J., 1963. The characteristics of the turbulence in the mixing region of a round jet. J. Fluid Mech. 15, 337–367.
Fleury, V., 2006. Superdirectivité, bruit d'appariement et autres contributions au bruit de jet subsonique. PhD Thesis, Ecole Centrale de Lyon.
Fleury, V., Bailly, C., Jondeau, E., Michard, M., Juvé, D., 2008. Space–time correlations in two subsonic jets using dual particle image velocimetry measurements. AIAA J. 46 (10), 2498–2509.
Harper-Bourne, M., Fisher, M.J., 1973. The noise from shock waves in supersonic jets. AGARD CP, 131.
Henry, C., Bailly, C., Bodard, G., 2012. Statistical Modeling of BBSAN including Refraction Effects. AIAA Paper 2012-2163.
Jerónimo, A., Riethmuller, M.L., Chazot, O., 2002. PIV application to Mach 3.75 overexpanded jet. In: 11th International Symposium on Applications of Laser Techniques to Fluid Mechanics, Lisbon.
Jordan, P., Gervais, Y., Valière, J.-C., Foulon, H., 2002. Jet Exhaust Aerodynamics and Noise. E.U. Research Project Jean Deliverable 3.4.
Kerhervé, F., Jordan, P., Gervais, Y., Valière, J.-C., Braud, P., 2004. Two-point laser Doppler velocimetry measurements in a Mach 1.2 cold supersonic jet for statistical aeroacoustic source model. Exp. Fluids 37 (3), 419–437.
Lau, J.C., 1980. Laser velocimeter correlation measurements in subsonic and supersonic jets. J. Sound Vib. 70 (1), 85–101.
Lau, J.C., 1981. Effects of exit Mach number and temperature on mean-flow and turbulence characteristics in round jets. J. Fluid Mech., 105.
Laurence, J.C., 1956. Intensity, Scale, and Spectra of Turbulence in Mixing Region of Free Subsonic Jet, NACA Report 1292.
Mahadevan, R., Loth, E., 1994. High-speed cinematography of compressible mixing layers. Exp. Fluids 17 (3), 179–189.
Michalke, A., 1965. On spatially growing disturbances in an inviscid shear layer. J. Fluid Mech. 23 (3).
Morris, P.J., Miller, S.A.E., 2010. Prediction of broadband shock-associated noise using Reynolds-Averaged Navier–Stokes computational fluid dynamics. AIAA J. 48 (12), 2931–2943.
Norum, T.D., Seiner, J.M., 1982. Measurements of Mean Static Pressure and Far Field Acoustics of Shock Containing Supersonic Jets. NASA Technical Memorandum 84521.
Norum, T.D., Shearin, J.G., 1988. Shock Structure and Noise of Supersonic Jets in Simulated Flight to Mach 0.4, NASA Technical Paper 2785.
Panda, J., 1999. An experimental investigation of screech noise generation. J. Fluid Mech. 378, 71–96.
Panda, J., 2006. Two Point Space–Time Correlation of Density Fluctuations measured in High Velocity Free Jets. AIAA Paper 2006-0006.
Panda, J., Seasholtz, R.G., 1999. Measurement of shock structure and shock-vortex interaction in underexpanded jets using Rayleigh scattering. Phys. Fluids 11 (12), 3761–3777.
Pao, S.P., Seiner, J.M., 1983. Shock-associated noise in supersonic jets. AIAA J. 21 (5), 687–693.
Papamoschou, D., Roshko, A., 1988. The compressible turbulent shear layer: an experimental study. J. Fluid Mech. 197 (1), 453–477.

Ponton, M.K., Seiner, J.M., 1992. The effects of nozzle exit lip thickness on plume resonance. J. Sound Vib. 154 (3), 531–549.
Powell, A., 1953. On the mechanism of choked jet noise. Proc. Phys. Soc. Lond., Sect. B 66 (12), 1039–1056.
Seiner, J.M., Norum, T.D., 1979. Experiments on Shock Associated Noise of Supersonic Jets. AIAA Paper 79-1526.
Seiner, J.M., Norum, T.D., 1980. Aerodynamic Aspects of Shock Containing Jet Plumes. AIAA Paper 80-0965.
Seiner, J.M., Yu, J.C., 1984. Acoustic near-field properties associated with broadband shock noise. AIAA J. 22 (9), 1207–1215.
Seiner, J.M., Dash, S.M., Wolf, D.E., 1985. Analysis of turbulent underexpanded jets. Part II: Shock noise features using SCIPVIS. AIAA J. 23 (5), 669–677.
Tam, C.K.W., 1987. Stochastic model theory of broadband shock-associated noise from supersonic jets. J. Sound Vib. 116 (2), 265–302.
Tam, C.K.W., Tanna, H.K., 1982. Shock associated noise of supersonic jets from convergent–divergent nozzles. J. Sound Vib. 81 (3), 337–358.
Troutt, T.R., McLaughlin, D.K., 1982. Experiments on the flow and acoustic properties of a moderate-Reynolds-number supersonic jet. J. Fluid Mech., 116.
White, F.M., 1974. Viscous Fluid Flow. McGraw Hill.